

# Tuning of Structural and Magnetic Properties of SrSnO<sub>3</sub> Nanorods in Fabrication of Blocking Layers for Enhanced Performance of Dye-Sensitized Solar Cells

Theanmozhi Mohan, Sasikumar Kuppusamy, and Robin Jude Vimal Michael\*



Cite This: *ACS Omega* 2022, 7, 18531–18541



Read Online

ACCESS |



Metrics & More

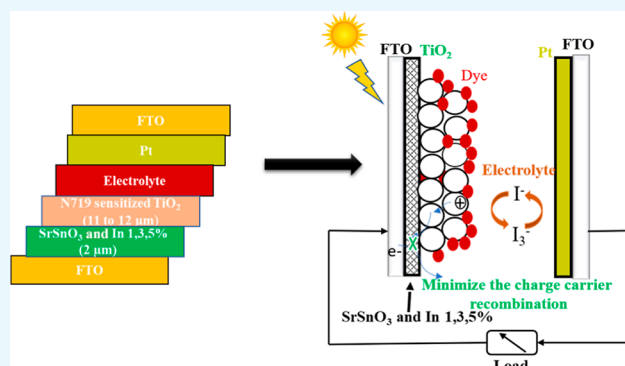


Article Recommendations



Supporting Information

**ABSTRACT:** Perovskite-based SrSnO<sub>3</sub> nanostructures doped with indium are prepared via a facile chemical precipitation method. Prepared nanostructures are used to assemble the dye-sensitized solar cells (DSSCs), and their photovoltaic response and electrochemical impedance spectra are measured. The synthesized samples are subjected to structural, morphological, optical, and magnetic properties. The X-ray diffraction pattern confirms the single-phase orthorhombic (Pbnm) perovskite structure. Local structural and phonon mode variations are examined by Raman spectra. Electron micrographs disclose the nanorods. The elements (Sr, Sn, O, and In) and the existence of oxygen vacancies are identified by X-ray photoelectron spectroscopy analysis. Surface area analysis demonstrates the higher surface area (11.8 m<sup>2</sup>/g) for SrSnO<sub>3</sub> nanostructures. Optical absorption spectra confirm the good optical behavior in the ultraviolet region. The multicolor emission affirms the presence of defects/vacancies present in the synthesized samples. The appearance of interesting ferromagnetic behavior in the prepared samples is due to the presence of F-center exchange interactions. Under the irradiation (1000 W/m<sup>2</sup>) of simulated sunlight, the DSSC fabricated by 3% In-doped SrSnO<sub>3</sub> exhibits the highest  $\eta$  of 5.68%. Hence, the blocking layers prepared with pure and indium-doped samples could be the potential candidates for DSSC applications.



## INTRODUCTION

Dye-sensitized solar cells (DSSCs) are the promising candidates for alternate solid-state junction solar cells, which have greater photo-to-electric power conversion efficiency, are less expensive and ecologically friendly.<sup>1–3</sup> Oxide-based perovskites are more stable and have received a great deal of attention because of their wide range of advantages compared to binary oxides such as ZnO, SnO<sub>2</sub>, and TiO<sub>2</sub> in order to modify their physio-chemical properties.<sup>4–6</sup> Several electrode materials are studied and applied to energy productions, storage and fuel cells with novel materials are reported earlier.<sup>7–9</sup> In recent years, perovskite-structured oxides (ABO<sub>3</sub>) have become more fascinating and have received greater research interest owing to their intriguing physical features and potential applications in various fields such as electrodes, catalysts, and sensors. Perovskites have extensively been studied in terms of synthesis methods, structural, and physio-chemical properties.<sup>10–12</sup> The oxides that are being explored for DSSC applications (SrTiO<sub>3</sub>,<sup>13</sup> Zn<sub>2</sub>SnO<sub>4</sub>,<sup>14</sup> CdSnO<sub>3</sub>,<sup>15</sup> and BaSnO<sub>3</sub><sup>16</sup>). Stimulatingly, the stannate-based compounds deliver good photovoltaic properties. Zinc stannate (Zn<sub>2</sub>SnO<sub>4</sub>) has an efficiency of 3.7%,<sup>14</sup> for CdSnO<sub>3</sub> is 1.1%,<sup>15</sup> and BaSnO<sub>3</sub> is ~1.42%,<sup>16</sup> respectively. Amid various stannate-based perovskites, SrSnO<sub>3</sub> has high electrical

conductivity and good thermal stability. It is broadly studied for photoluminescence (PL)-based applications. Li et al. fabricated and certified that SrSnO<sub>3</sub> could be a suitable anode material to increase the DSSC performance in the current stage.<sup>17</sup> Therefore, greater efforts are required to develop a suitable anode material. However, the addition of dopants and synthesis methods are proven effective ways to get higher efficiency.

The transition and rare earth (RE) elements are doped into the Sr–Sn–O lattice, resulting in a material with a significant influence on optical and magnetic properties.<sup>17–21</sup> Moreover, the RE elements are used in various fields because of their excellent optical conversion efficiency and stable physio-chemical properties.<sup>17,18</sup> Recent studies<sup>18</sup> demonstrate that the up/down conversion ability of RE ions might enhance the spectral response of DSSCs from the visible to ultraviolet (UV) or infrared (IR) region. Samarium (Sm<sup>3+</sup>) ions might be the

Received: February 28, 2022

Accepted: May 18, 2022

Published: May 27, 2022



most effective down-converting material, which converts the UV to visible emissions so that light might get reabsorbed by dyes.<sup>19</sup> The SrSnO<sub>3</sub> nanoparticles deposited by the chemical bath deposition delivered an enhanced efficiency (1.90%) through solar radiation significantly.<sup>20</sup> The efficiency of DSSCs could be increased by selecting suitable materials for the blocking layer and optimizing their conditions. The role of blocking layers has been extensively researched and reported.<sup>22–26</sup> Cho et al. reported that the blocking layer of Nb<sub>2</sub>O<sub>5</sub> might augment the efficacy of DSSCs.<sup>22</sup> When TiO<sub>2</sub> is used as a blocking layer due to enhanced electron lifetime, the photovoltaic conversion efficiency of 27% is achieved.<sup>23</sup> The core–shell structure of SnO<sub>2</sub>–CdO delivers an enhanced efficiency in DSSCs. The shell thickness also plays a greater role in the performance of the DSSC.<sup>24</sup> Enhanced performance in perovskite solar cells through Ta, the Nb-doped TiO<sub>2</sub> blocking layer is reported by Song et al.<sup>25</sup> Moreover, Wei et al. reported that the greater performance of the DSSC while using RGO/TiO<sub>2</sub> as a blocking layer.<sup>26</sup> Recently, Kumar et al. reported that the influence of the thickness variation effect of the TiO<sub>2</sub> film, prepared by the surfactant-assisted template synthesis method for improved DSSC efficiency.<sup>27</sup>

Photocurrent responsiveness and catalytic efficacies are influenced by the nature of cations, crystal shape and size, and surface area. These entities can be tailored by synthesis methods.<sup>28</sup> To attain the enhanced response, the samples should have a uniform microstructure and be free from impurities. Various chemical synthesis methods are reported in order to synthesize SrSnO<sub>3</sub> nanostructures, such as sol–gel,<sup>29</sup> hydrothermal,<sup>30</sup> chemical precipitation,<sup>31</sup> microemulsion,<sup>32</sup> and solid-state reaction (SSR) processes.<sup>33</sup> Among the different powder fabrication processes, solution-based procedures are simple, and the reaction temperature is lower than that of SSRs. In the ABO<sub>3</sub> structure, doping at the B site enhances the photoactivity.<sup>34</sup> However, more works on transition, RE, and semimetals are recorded but indium-doped SrSnO<sub>3</sub> for DSSC applications is seldom studied and reported.

Hence, pure and indium (In)-doped SrSnO<sub>3</sub> are prepared by the chemical precipitation method and examined for their structural, optical, morphological, and magnetic properties. The photocurrent–voltage is measured for the fabricated DSSCs with synthesized samples, then the efficiency is calculated and reported.

## EXPERIMENTAL METHODS

**Materials and Methods.** For the preparation of pure and indium (1, 3, and 5%)-doped SrSnO<sub>3</sub>, the chemical precipitation method is employed, where analytical grade Sr(NO<sub>3</sub>)<sub>2</sub>, Na<sub>2</sub>SnO<sub>3</sub>·3H<sub>2</sub>O, InCl<sub>3</sub>, and polyethylene glycol (PEG 400) are used as starting materials. The stoichiometric amounts of Sr(NO<sub>3</sub>)<sub>2</sub> and Na<sub>2</sub>SnO<sub>3</sub>·3H<sub>2</sub>O are dissolved in deionized (DI) water. Then, the strontium nitrate solution is added dropwise into the sodium stannate solution through continual stirring to get a homogeneous solution. After that, PEG of 0.1 M was added. Then, the pH is measured and maintained at 8–9 and the solution is continuously stirred for 5 h, then left to age for 12 h. Furthermore, the precipitation is washed with DI water and solvents such as ethanol and acetone subsequently, and then permitted to be parched at ambient temperature. Thenceforth, the products are ground into fine powders and calcined at 900 °C for 4 h. To synthesize indium-doped SrSnO<sub>3</sub>, a stoichiometric quantity of the indium

chloride solution is added into the sodium stannate solution, and then a similar procedure is followed. The final products are subjected to various physio-chemical characterizations.

**Assembly of DSSCs.** Fluorine-doped tin oxide (FTO) substrates are cleaned with acetone, ethanol, and distilled water, followed by 20 min of ultrasonication. The UV-treated (15 min) FTO substrates are masked by scotch tape to define the active device area for photoanode preparation. The doctor blade technique is used to coat the P25 Degussa TiO<sub>2</sub> paste on FTO substrates for photoanode preparation (thickness ranging from 11 to 12 μm). The prepared photoanodes are annealed at 500 °C for 30 min and treated to a dye-sensitization process for 12 h, during which ethanolic N719 (0.5 mM) dye is utilized to sensitize the photoanodes. These photoanodes are splashed with ethanol (anhydrous) to eliminate the unanchored particles of dye. To prepare the counter electrodes, a quantity of chloroplatinic acid (20 mM) was dispersed in ethanol and coated on FTO substrates by the spin-coating method. The spin-coated Pt-based counter electrodes are heated for 500 °C/10 min. To prepare the standard iodine-based liquid electrolyte, required quantities of PMMI = 0.7 M, I<sub>2</sub> = 0.05 M, tBP = 0.5 M, and GuSCN (0.03 M) in 20 mL of acetonitrile are used and optimized. Finally, the prepared liquid electrolyte is filled in the drilled holes of the counter electrode and sealed using a Surlyn spacer.<sup>35</sup>

For pure and indium-doped SrSnO<sub>3</sub>-based DSSCs, the prepared sample was dissolved in dimethylformamide (DMF) (10 mg of the sample in 1 mL of DMF) and spin coated as the bottom layer (before coating TiO<sub>2</sub>) of the photoanode at 3000 rpm for 40 s (as the blocking layer ~ thickness 2 μm).

**Materials Characterizations.** X-ray diffraction (XRD) patterns are measured using an X-ray diffractometer (Bruker D8) using Cu Kα radiation. Rietveld refinements are performed using the GSAS program through a pseudo-Voigt peak. IR modes are identified (4000–400 cm<sup>-1</sup>) using an IR spectrometer (Thermo Nicolet-6700). The Raman spectra of 100–1000 cm<sup>-1</sup> are recorded using the HORIBA scientific lab ram spectrometer. An electron microscope (FE-SEM-JSM-7100, JEOL, Japan) (JEOL JEM 2100) is used to detect the surface morphology. ESCALAB 250 (Al Kα radiation) is used to perform the X-ray photoelectron spectroscopy (XPS) analysis. Thermo Electron Corporation, USA. Surface area and pore size distributions are examined using BELSORP Microtrac MINI-II. UV–visible spectroscopy is measured (200–800 nm) using the spectrophotometer Shimadzu UV2450. A HORIBA Jobin Yvon FL311 Fluorolog-3 spectrophotometer (excitation of 290 nm) is used to find the PL emissions. The magnetic response against the field is measured using a vibrating sample magnetometer (VSM) by Lake Shore (7407). Current density–voltage (*J*–*V*) measurements were studied using a standard solar simulator (Polaronix K201, McScience, Korea) under 1 sun intensity (AM 1.5 G filter). An electrochemical impedance spectroscopy (EIS) measurement was carried out using the VersaSTAT 4 electrochemical workstation (Princeton Applied Research, USA).

## RESULTS AND DISCUSSION

**Phase Analysis.** The XRD refined patterns of pure and indium-doped SrSnO<sub>3</sub> nanostructures are depicted in Figures 1, 2, and S1.

The diffraction patterns are in accordance with the orthorhombic structure (JCPDS:77-1798, which denotes

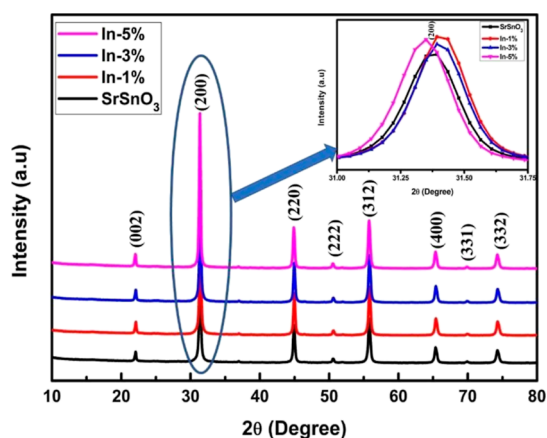


**Figure 1.** XRD pattern of pure and indium-doped SrSnO<sub>3</sub> nanostructures.

perovskite SrSnO<sub>3</sub>), and exhibits no trace of impurities. The maximum intensity plane (220) is shifted toward a higher angle on the introduction of indium ions. As the concentration of indium increases, the diffraction patterns are shifted toward a lower angle. This could be attributed to the crystallographic reconstruction of SrSnO<sub>3</sub>.<sup>36,37</sup> However, the doped (In) samples do not show any indium-related content in diffracted patterns, which suggests that indium ions are incorporated into the Sr–Sn–O lattice.

The mean crystallite size and strain components are estimated by the *W–H* plot.

$$\beta_{(hkl)} \cos \theta_{(hkl)} = K\lambda/D + 4\epsilon \sin \theta_{(hkl)} \quad (1)$$

Here,  $D \sim$  mean crystallite size,  $\lambda \sim$  Cu K $\alpha = 0.15418$  nm wavelength of X-rays,  $K \sim 0.9$  shape factor, and  $\beta \sim$  full width at half-maximum of peak at  $2\theta$ , and  $\epsilon \sim$  strain.<sup>36</sup>

The strain induced in the lattice is calculated using the *W–H* equation and the plot is made and shown in Figure S2. The calculated strain, crystallite size, and lattice parameter values are enumerated in Table 1.

The table discloses that the lattice constants “a” and “c” increases, whereas “b” decreases, this suggests that the unit cell elongated at the “a and c” directions, and gets contracted at the “b” direction, in order to retain the crystal structure. Furthermore, the unit cell volume increases on increasing the indium concentration; this is ascribed to the dopants (In) diffused in the Sr–Sn–O matrix. The strain and crystallite size values show the inverse relationship between them, and this discrepancy in the crystallite size and strain are due to differences in their ionic radius (Sr = 1.32 Å, Sn = 0.69 Å, and In = 0.8 Å). On photocatalytic perception, if the lattice defects are minimized, the recombination rate of photogenerated charge carriers also decreases. In general, lattice defects induce strain in prepared nanostructures. These lattice defects will act as traps for photoexcited charge carriers, which will lead to a decrease in efficiency. In the present work, Rietveld refinement clearly shows the minimized lattice defects in the prepared samples. Hence, the XRD pattern confirmed that the dopant (In) ions interact and perturb the Sr–Sn–O matrix without affecting the crystal structure.<sup>38</sup>

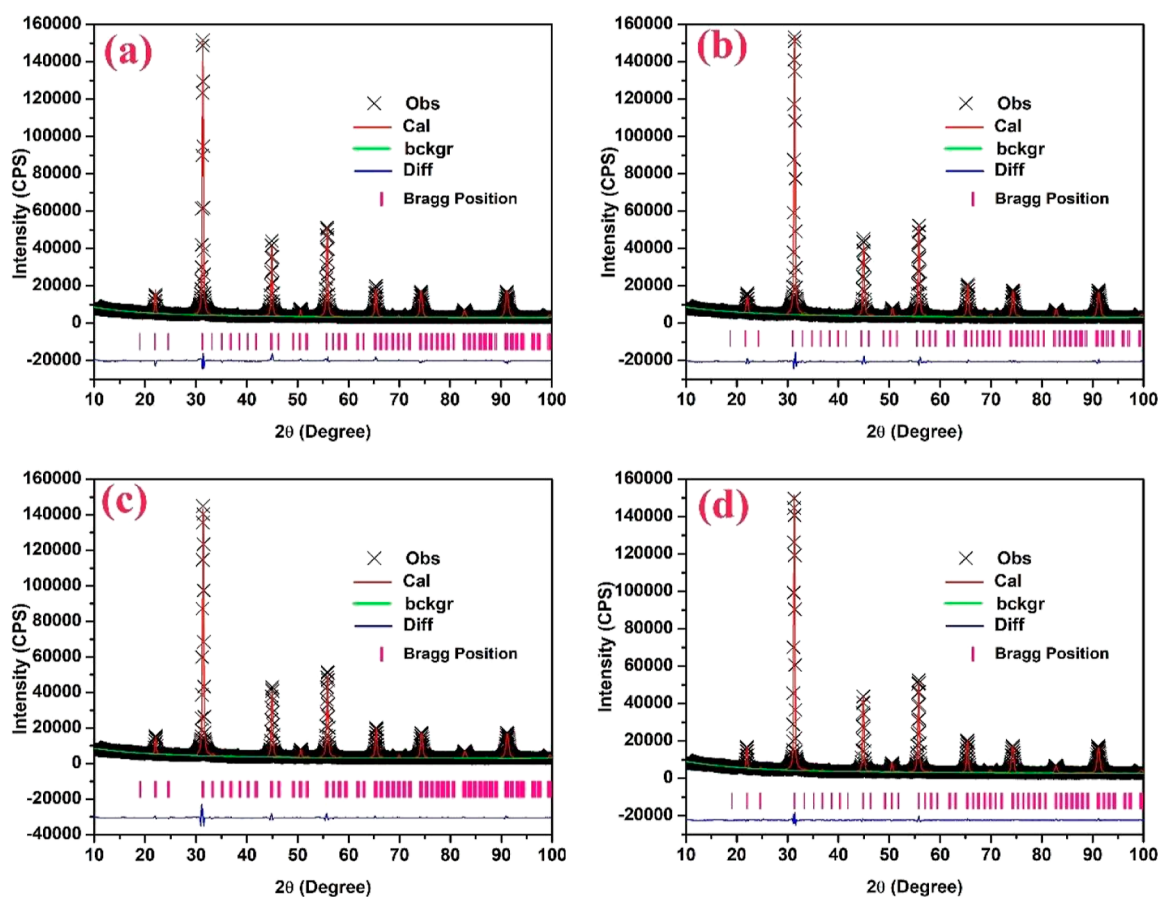


**Figure 2.** Rietveld refinement of pure and indium-doped SrSnO<sub>3</sub>, (a) pristine SrSnO<sub>3</sub>, (b) In-1%, (c) In-3%, and (d) In-5%.

Table 1. Refined Crystallographic Parameters and Atomic Parameters of Pure and Indium-Doped SrSnO<sub>3</sub> Nanostructures

sample	SrSnO <sub>3</sub>	In-1%	In-3%	In-5%
crystal system	orthorhombic	orthorhombic	orthorhombic	orthorhombic
space group	<i>Pbnm</i>	<i>Pbnm</i>	<i>Pbnm</i>	<i>Pbnm</i>
lattice parameters	<i>a</i> = 5.7107(5) Å <i>b</i> = 5.7206(4) Å <i>c</i> = 8.0685(5) Å $\alpha = \beta = \gamma = 90^\circ$	<i>a</i> = 5.7129(6) Å <i>b</i> = 5.7140(6) Å <i>c</i> = 8.0724(8) Å $\alpha = \beta = \gamma = 90^\circ$	<i>a</i> = 5.7148(7) Å <i>b</i> = 5.7159(6) Å <i>c</i> = 8.0928(9) Å $\alpha = \beta = \gamma = 90^\circ$	<i>a</i> = 5.7199(5) Å <i>b</i> = 5.7145(4) Å <i>c</i> = 8.177(5) Å $\alpha = \beta = \gamma = 90^\circ$
unit cell volume (Å <sup>3</sup> )	<i>V</i> = 263.583(7)	<i>V</i> = 263.592(6)	<i>V</i> = 263.84(6)	<i>V</i> = 264.20(4)
<i>R<sub>p</sub></i> (%)	3.11	2.79	2.95	1.98
<i>R<sub>wp</sub></i> (%)	4.29	3.99	4.42	2.79
$\chi^2$ (%)	1.08	1.23	1.83	1.26
strain	0.00174	0.00161	0.00273	0.00261
crystallite size (nm) <i>W-H</i> plot	55	51	50	53

**Fourier Transform Infrared and Raman Investigations.** The Fourier transform IR (FTIR) analysis of pure and indium-doped SrSnO<sub>3</sub> nanostructures is given in Figure 3.

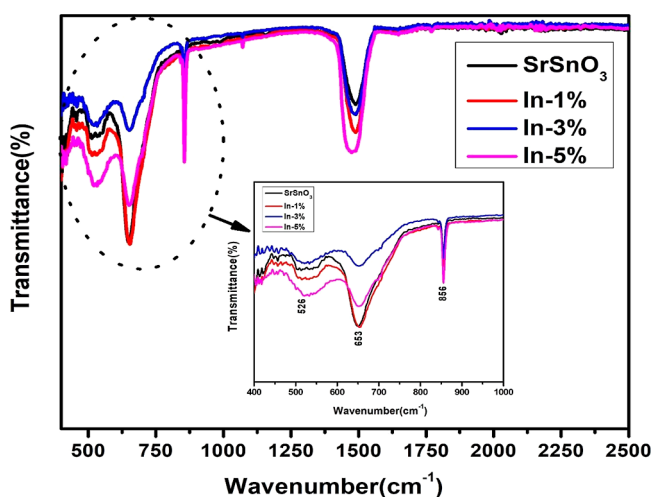


Figure 3. FTIR spectra of pure and indium-doped SrSnO<sub>3</sub> nanostructures.

The mode at 526 cm<sup>-1</sup> represents the stretching vibrations of Sn–O metal oxides. The band at 653 cm<sup>-1</sup> is related to the (SnO<sub>3</sub><sup>2-</sup>) vibrations. The peak at 856 cm<sup>-1</sup> denotes the molecular vibrations of Sn–O.<sup>38,39</sup> Bands at 1476 cm<sup>-1</sup> are allotted to carbonate-related symmetric axial deformation. Hence, the FTIR spectra affirmed the metal oxide (M–O) vibrations existed in the synthesized nanostructures.

The laser Raman spectra are used to examine the structural purity and identify the local structural disorders in the compounds.<sup>39</sup> The Raman spectra of SrSnO<sub>3</sub> and indium-doped SrSnO<sub>3</sub> are depicted in Figure 4.

Identified Raman modes (114, 147, 170, 223, 257, 404, and 570 cm<sup>-1</sup>) are in accordance with earlier reported values.<sup>40</sup> The A<sub>g</sub> Raman mode of SrSnO<sub>3</sub> is assigned to 223 and 257 cm<sup>-1</sup>. The scissoring vibrations of Sn–O–Sn through the C-axis exhibit the intense peak at 223 cm<sup>-1</sup> as reported by Moreira et al.<sup>41</sup> The bending motion of the O–Sn–O, B<sub>2g</sub> mode, and the (Sn–O–Sn) scissoring motions are perpendicular to the *c*-axis, which is identified by the peak at 257 cm<sup>-1</sup>. The Sr–SnO<sub>3</sub> vibrations are detected by the existence of low intensity modes at 114, 147, and 170 cm<sup>-1</sup>. The SnO<sub>3</sub> torsional mode is indicated by the peak 404 and 570 cm<sup>-1</sup>, which is associated with stretching (Sn–O) vibrations. Distinctively,

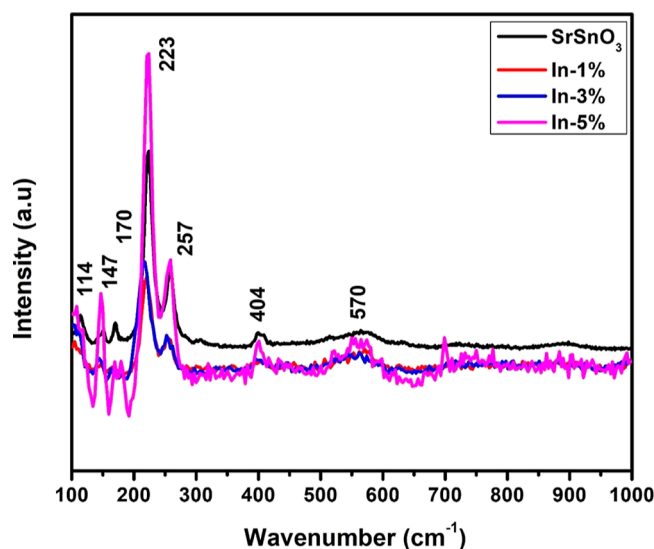


Figure 4. Raman spectra of pure and indium-doped SrSnO<sub>3</sub> nanostructures.

the torsional mode of SnO<sub>3</sub> at 570 cm<sup>-1</sup> provides the substantial (SnO<sub>6</sub> octahedra) structural information.<sup>42</sup> Thus, Raman studies affirm the crystal system is unaltered by indium ions, but there is a small shift in modes that reveals the indium ions perturb the Sr–Sn–O lattice considerably.

**Electron Microscopic Analysis.** Field emission-scanning electron microscopy (FE-SEM) images of SrSnO<sub>3</sub> and 5% In-doped SrSnO<sub>3</sub> compounds, corresponding the elemental analyses are given in Figure 5a,b. From the micrographs, it is noted that pure SrSnO<sub>3</sub> has a bundle of rods with a size of 180 nm approximately, which is tightly packed and uniformly dispersed.<sup>36</sup> The dopant atoms (In) are diffused in the lattice and induce considerable variation in the rod size (~200 nm). Energy-dispersive X-ray spectroscopy (EDS) of pure and indium-doped samples are disclosed in Figure 5a and b, which reveal the quantitative atomic percentage of elements such as Sr, Sn, and O. Furthermore, the EDS analysis of doped samples confirms the existence of indium ions in the Sr–Sn–O lattice.

The electron micrograph of SrSnO<sub>3</sub> and In-5% doped nanostructures are shown in Figure 6. Figure 6 also confirms the formation of rods<sup>36</sup> and some of the smaller-sized particles of SrSnO<sub>3</sub> can be found on the surface of the rod. The typical surface area electron diffraction pattern exhibits concentric rings, which suggest the polycrystalline nature of compounds. The obtained reflections are from the crystallographic planes of

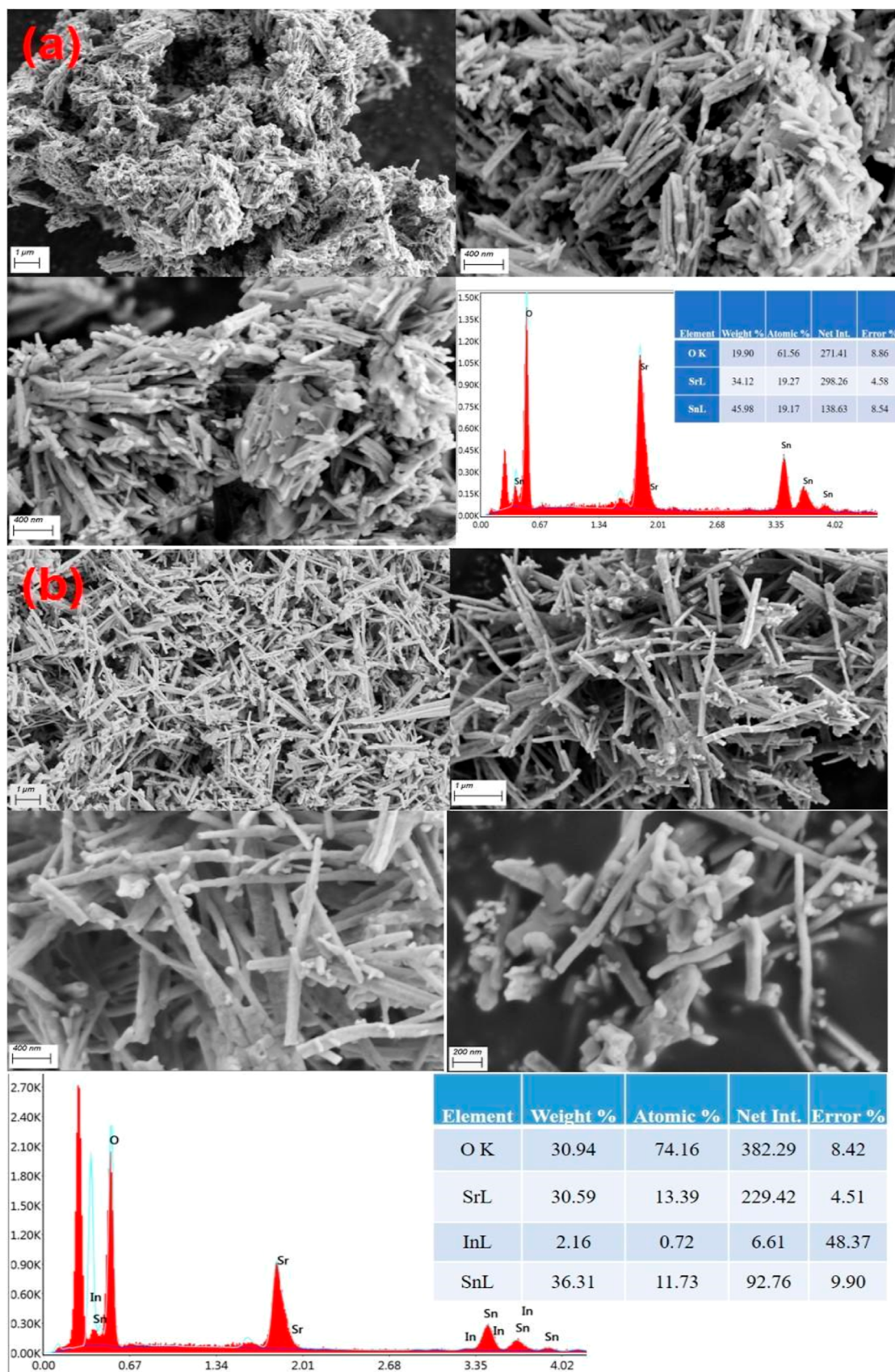
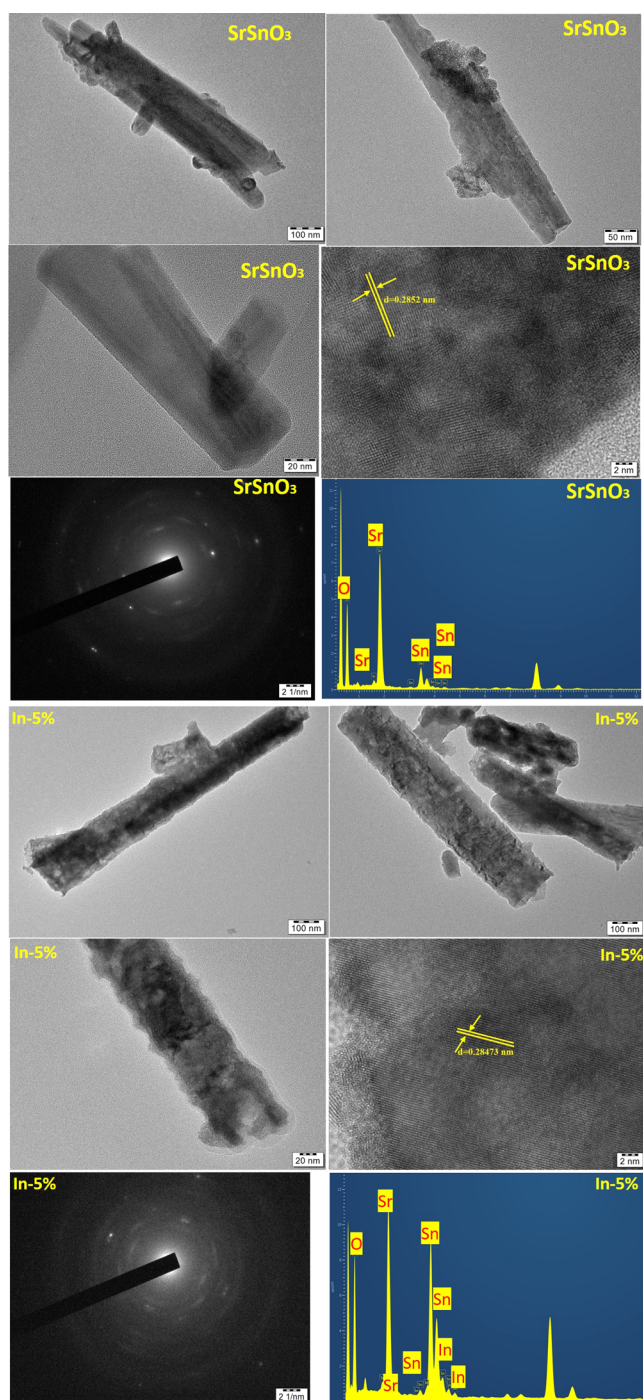


Figure 5. FE-SEM images with energy-dispersive X-ray analysis, (a) pure SrSnO<sub>3</sub> and (b) In-5% doped SrSnO<sub>3</sub> nanostructures.



**Figure 6.** High-resolution TEM images of pure and In-5% doped  $\text{SrSnO}_3$  nanostructures.

orthorhombic  $\text{SrSnO}_3$  compounds. Transmission electron microscopy (TEM) investigations reveal both shape and size are consistent with XRD and SEM analysis.

**XPS Analysis.** The typical survey spectra containing the surface elements of Sr 3d, Sr 3p, Sn 3d, O 1s, and In 3d are shown in Figure 7a–i. The spectra are calibrated with the binding energy of C 1s (284.8 eV). The survey spectra illustrated that there is no impurity element in the prepared  $\text{SrSnO}_3$ . The inspection of Sr 3d and Sn 3d indicates that Sr is in a +2 valence state, and Sn ions are in a +4 state.<sup>12,36,42</sup> The detailed region scans of Sr 3d, Sn 3d, and O 1s for all the samples in Figure 7a–i. The Sr 3d peaks for pure  $\text{SrSnO}_3$ ,

compounds are assigned to Sr  $3d_{5/2}$   $\sim$  131.76 eV and Sr  $3d_{3/2}$   $\sim$  134.26 eV with 2.5 eV peak separation. The indium-doped Sr 3d shows a peak at 131.95 eV for  $3d_{5/2}$  and  $3d_{3/2}$   $\sim$  134.49 eV with a separation of 2.54 eV. This authorizes the +2 state of Sr. The modification in B. E (Sr 3d) is due to the distribution of indium in the Sr–Sn–O matrix.

The XPS spectra of Sn 3d of pure  $\text{SrSnO}_3$  displays two peaks at 495.5 eV for  $3d_{3/2}$  and 487.2 eV for  $3d_{5/2}$ , with a peak difference of 8.3 eV. Similarly, indium-doped Sn exhibits the peak at 494.3 eV for  $3d_{3/2}$  and 485.9 eV for  $3d_{5/2}$  with a separation of 8.4 eV. This difference in B. E suggests that the Sn is in a +4 oxidation state. For the O 1s spectra, asymmetric peaks are observed with binding energies of 528.7, 531, and 533 eV for pure samples, and 529.9 and 532.4 eV for indium-doped samples. This may be attributed to lattice and surface oxygen vacancies, respectively. In order to maintain the charge neutrality enhanced oxygen vacancy is observed at indium-doped samples. The In-5% doped samples have shown the spin–orbit binding energy component at 443.33 eV (In  $3d_{5/2}$ ) and 450.93 (In  $3d_{3/2}$ ), which confirms the +3 oxidation state of In. Hence, XPS examination confirms the presence of oxygen vacancies and corresponding oxidation states in prepared samples.

**Surface Area Analysis.** The nitrogen adsorption–desorption spectra of the prepared pure and indium-doped  $\text{SrSnO}_3$  nanostructures are revealed in Figure 8a. The Brunauer–Emmett–Teller (BET) surface area, pore volumes, and pore radius are given in Table 2. According to the IUPAC classification, the isotherms of synthesized nanomaterials deliver a type IV hysteresis curve of typical mesoporous materials by ink-bottle pores (H2 type). The pore size distributions (6.28 to 2.68 nm) of pure and indium-doped  $\text{SrSnO}_3$  samples are calculated by the Barrett–Joyner–Halenda method and shown in Figure 8b.

The highest pore radius and pore volume are observed for pure samples. The pore radius and pore volumes decrease as a function of indium concentrations. The surface area value decreases with increases in the indium concentration (11.8 to 7.37  $\text{m}^2/\text{g}$ ). Moreover, the surface area values are higher than those of  $\text{SrSnO}_3$  produced by the SSR (2.8  $\text{m}^2/\text{g}$ ), microwave-assisted hydrothermal method (6.6  $\text{m}^2/\text{g}$ ), and microwave-assisted ionic liquid method.<sup>43</sup> Hence, from the surface area measurement, it is noted that the prepared compounds possess a high surface area and might enhance the physical properties of pure and indium-doped samples.

**Optical Absorption Studies.** The absorption spectra of  $\text{SrSnO}_3$  samples with different indium concentrations are shown in Figure 9.

The absorption peak between 210 and 310 nm is ascribed to oxygen–metal (M–O) charge-transfer transitions.<sup>36,44</sup> The absorption behavior discloses the impact of strain, size, and shape of crystallites. In particular, the strain leads to surface/interface traps and localized energy on the surfaces. On increasing indium concentration, a distinct shift appears due to the transitions between indium ions and the Sr–Sn–O matrix. The absorption behavior of the  $\text{SrSnO}_3$  compound also relies on the transition of O 2p to Sn 3d states.<sup>42</sup> From the earlier reports, the formation of intermediate energy levels within the forbidden gap and order-disorder parameters present in the host matrix could decrease the optical band gap value.<sup>34</sup> The band gap ( $E_g$ ) is affected by the synthesis process, surface morphology, temperature (calcination), and pH of the precursors. The oxygen vacancies, impurities/dopants, or

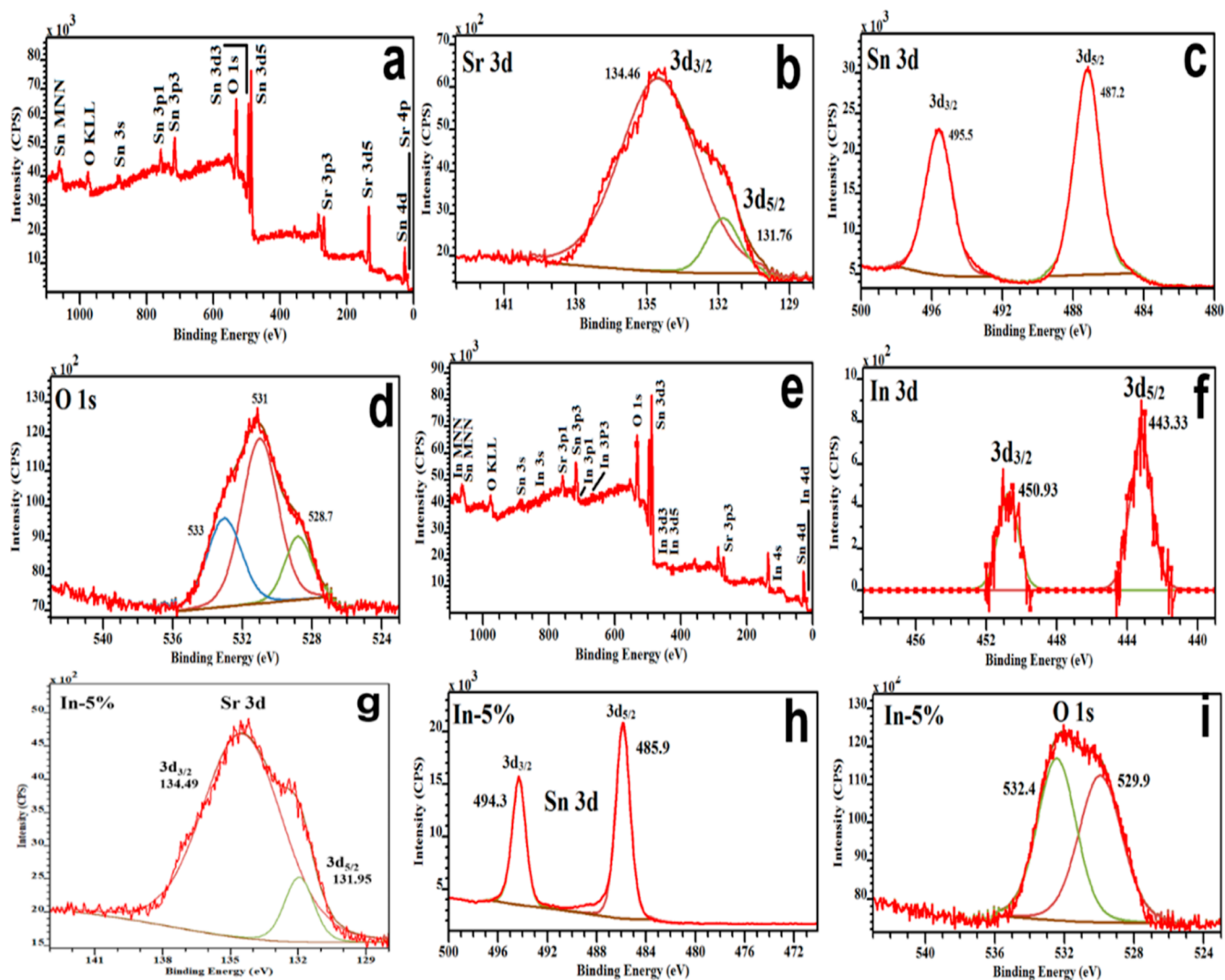


**Figure 7.** XPS of pure and In-5% doped  $\text{SrSnO}_3$  nanostructures (a,e) survey spectra, (b,g) Sr 3d state, (c,h) Sn 3d state, (d,i) O 1s state, and (f) In 3d state.

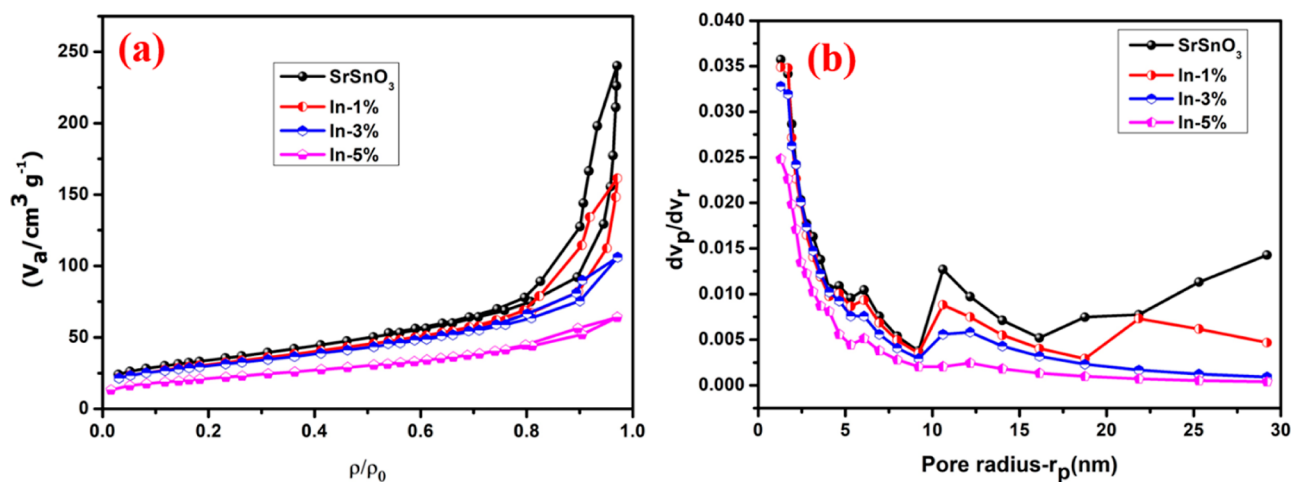


**Figure 8.** (a) Surface area analysis and (b) pore radius of pure and In-5% doped  $\text{SrSnO}_3$  nanostructures.

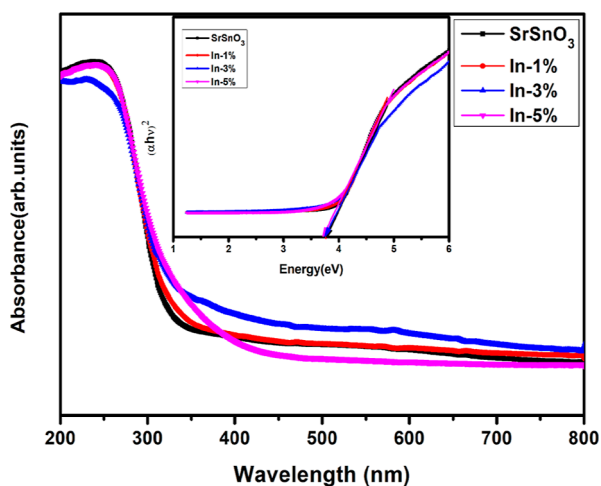
distortions might create an additional energy level in the forbidden energy bands of stannates.<sup>36</sup> The band gap ( $E_g$ ) is computed by the Tauc equation

$$\alpha h\nu = (h\nu - E_g)^n \quad (2)$$

where  $\alpha$  is absorbance,  $h$  is Planck's constant,  $\nu$  is frequency, and  $E_g$  is the optical band gap.<sup>36</sup> The absorption coefficient is

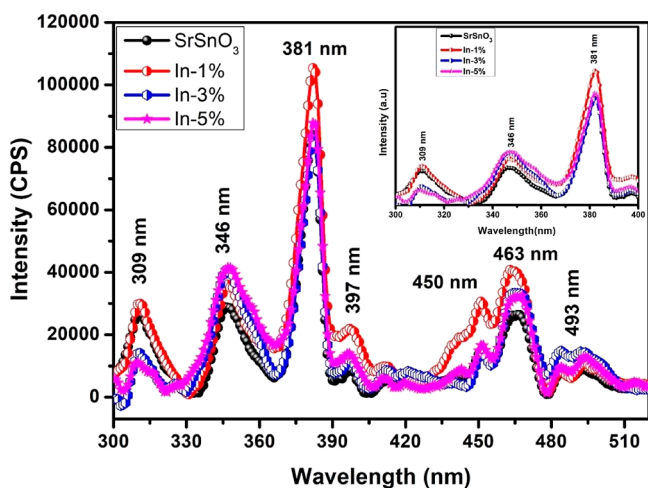
Table 2. Surface Area from BET Analysis

sample	surface area (m <sup>2</sup> /g)	pore volume, V <sub>p</sub> (cm <sup>3</sup> /g)	pore radius, r (Å)	optical band gap (eV) from Tauc plot
SrSnO <sub>3</sub>	11.8	0.3717	0.6289	3.76
In-1%	10.8	0.2497	0.4631	3.82
In-3%	10.6	0.1641	0.3074	3.80
In-5%	7.37	0.0991	0.2689	3.74

Figure 9. UV–visible spectra of pure and indium-doped SrSnO<sub>3</sub> nanostructures (inset-Tauc plot).

high, which denotes the direct allowed transition.<sup>44</sup> The graph is made between  $E_g$  and  $(\alpha h\nu)^2$  and depicted in the inset of Figure 9. The estimated band gap value is 3.72 eV for pure SrSnO<sub>3</sub>. Upon increasing the indium concentration, the  $E_g$  value is altered because of their crystalline, strain, and surface (shape and size) morphology.

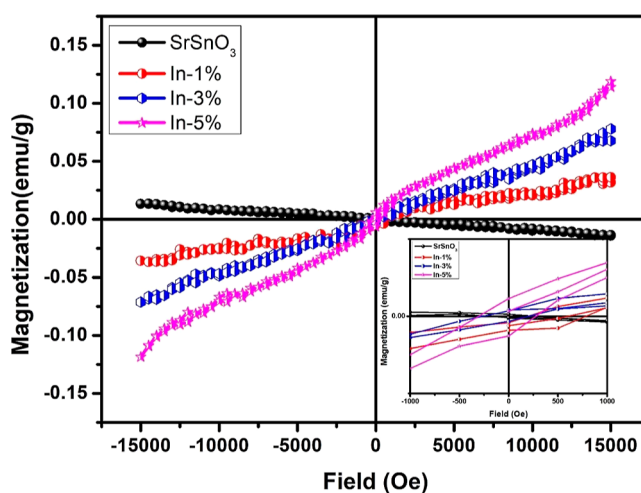
**Photoluminescence Studies.** The PL spectra (excited  $\lambda \sim 290$  nm) of pure and indium-doped SrSnO<sub>3</sub> nanostructures are portrayed in Figure 10. The emission at 381 nm represents the allowed direct transition between the energy levels of 2p of oxygen (O) and 5s of tin (Sn). The peaks at 309, 346, 381, 397, 450, 463, and 493 nm deliver the prepared samples containing defects and oxygen vacancies in the samples. The

Figure 10. PL spectra of pure and indium-doped SrSnO<sub>3</sub> nanostructures.

emission peaks of prepared nanostructures affirmed that the dopant does not alter the emission centers of the Sr–Sn–O lattice but reduces the characteristic emission intensities of SrSnO<sub>3</sub>. These reduced intensities are attributed to the presence of indium (In) ions enclosed by [SnO<sub>4</sub><sup>2-</sup>] groups.<sup>21,36</sup> The SrSnO<sub>3</sub> compose of octahedral and dodecahedral clusters [SnO<sub>6</sub>] and [SrO<sub>12</sub>], respectively.<sup>25,26</sup>

In general, the PL properties of the ABO<sub>3</sub>-structured materials are related to the presence of intermediated states inside the band gap because of the presence of oxygen vacancies, which induces falsifications in octahedral and dodecahedral clusters. These could act as recombination centers.<sup>21,22</sup> Furthermore, the PL emission also depends on surface morphology, calcination time, and temperature.<sup>42</sup> The dimensionality of the particles also has an impact on the luminescent behavior of SrSnO<sub>3</sub> structures.<sup>21</sup> Thus, PL spectra provide the details of the separation efficiency of the charge carriers. Typically, a higher emission intensity is correlated with an enhanced recombination rate and less activity. In the present work, it is noted that the introduction of indium suppresses the intensities of SrSnO<sub>3</sub>. The lower intensity PL peak suggested that the effective charge carrier's separation and thus an augmented photocatalytic activity could be expected.

**Magnetic Studies.** The magnetization curves obtained from a VSM for pure and indium-doped SrSnO<sub>3</sub> compounds are revealed in Figure 11.

Figure 11. Room temperature magnetic behavior of pure and indium-doped SrSnO<sub>3</sub> nanostructures.

A diamagnetic signature is observed for pure samples, but all the indium-doped samples depict ferromagnetic behavior. The ferromagnetic behavior of indium-doped samples is due to the presence of vacancies/defects and excess charge carriers produced by the indium ions. From the earlier reports,<sup>36,42</sup> transition metal-doped Cr and Fe-doped SrSnO<sub>3</sub> compounds demonstrated the induced ferromagnetic behavior and it is learned that the origin of ferromagnetic behavior in SrSnO<sub>3</sub> are explained on the basis of oxygen vacancies, defects, presence of F-center exchange interactions, and carrier-mediated ferromagnetism.

**Photovoltaic Device Application. J–V Curve.** The J–V curves for pure and indium-doped SrSnO<sub>3</sub> devices are illustrated in Figure 12.

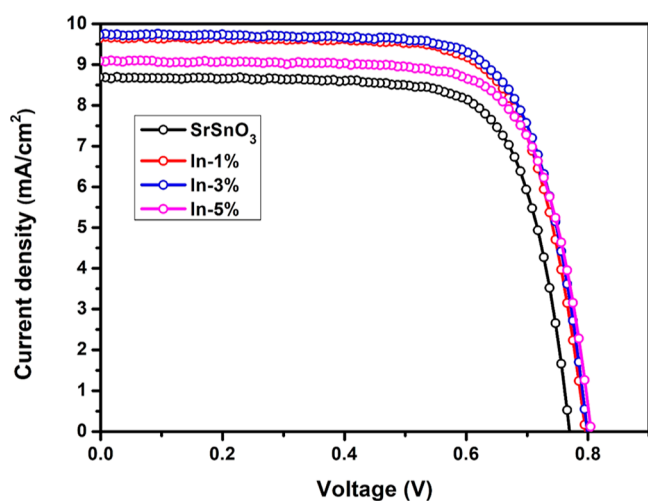


Figure 12.  $J$ - $V$  measurements of pure and indium-doped  $\text{SrSnO}_3$  nanostructures.

Detailed photovoltaic parameters are summarized in Table 3. The widely reported oxide-based blocking layers such as

Table 3.  $J$ - $V$  Parameters Derived from DSSCs

sample	$V_{oc}$ [V]	$J_{sc}$ [ $\text{mA}/\text{cm}^2$ ]	fill factor [%]	efficiency [%]
$\text{SrSnO}_3$	0.77	8.69	73.682	4.931
In-1%	0.796	9.648	73.065	5.611
In-3%	0.799	9.731	73.089	5.683
In-5%	0.805	9.09	73.233	5.358

$\text{TiO}_2$  and  $\text{Nb}_2\text{O}_5$  enhance the conversion efficiency. This opens a new window for the blocking layer research in oxide-based materials.<sup>22–26,28,35,45</sup> In the present work, perovskite-structured  $\text{SrSnO}_3$  is used as a blocking layer to study the effect of the photovoltaic response. Hence, from the results, it is noted that there is a considerable increase in the conversion efficiency.

From the table, it was noted that the current density gets enhanced for the indium-doped DSSC rather than the pure DSSC. In particular, 3% In-doped DSSCs resulted in a high power conversion efficiency (PCE) of 5.683% with an improved  $J_{sc}$  of 9.731  $\text{mA}/\text{cm}^2$  due to the optimal doping concentration of indium in  $\text{SrSnO}_3$  than the pure device (4.93%). Furthermore, the increased  $V_{oc}$  for doped DSSCs is due to the Fermi level shift (upshift) of the  $\text{SrSnO}_3/\text{TiO}_2$  photoanode. It can increase the potential difference between the Fermi level of the photoanode and the redox potential of the electrolyte and lead to an increase in the  $V_{oc}$  of the device. On the other hand, the high fill factor (FF) of nearly 73% was realized for all the DSSCs owing to the usage of the dielectric material as a blocking layer in the regular DSSC structure. It can reduce the back electron transfer and increase the charge transport process, which is confirmed by the EIS analysis. The FF also follows a similar trend for indium-doped samples.

**EIS Nyquist Plot.** EIS of DSSCs normally exhibits three kinds of carrier transport at the device interface by comprising three semicircle arcs in the Nyquist plot. The charge carrier transfer between the counter electrode and the electrolyte is represented by  $R_{ct}$ , charge transfer between the working electrode and the electrolyte is given by  $R_{rec}$ , and diffusion resistance at the photoanode is denoted by  $R_d$ . The objective of the current work is to focus on a new kind of anode and to

examine the electronic transport properties of photoanodes with the electrolyte ( $\text{I}^-/\text{I}_3^-$ ) and Pt counter electrodes.

Figure 13 represents the EIS Nyquist plot of fabricated DSSCs, which presents two semicircle arcs owing to the

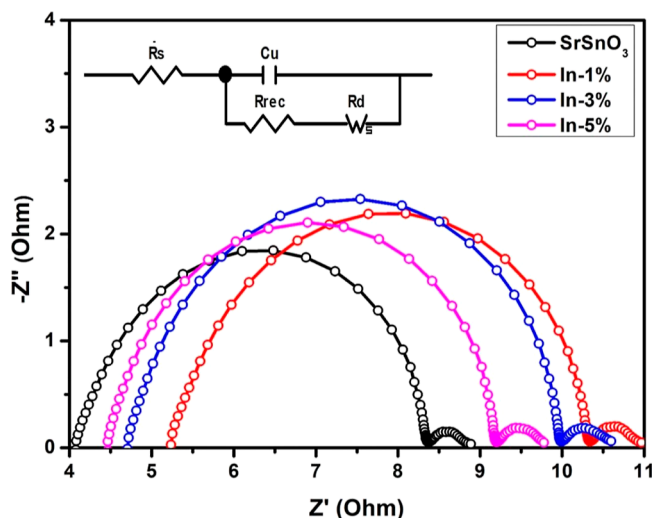


Figure 13. Electrochemical impedance spectra of pure and indium-doped  $\text{SrSnO}_3$  nanostructures.

electron transport at the photoanode/electrolyte interface which provides  $R_{rec}$ . The  $R_{ct}$  is similar for all the devices because of the usage of the similar counter electrode material and electrolyte, respectively. However, the contribution of  $R_{ct}$  is negligible due to the rapid electron transport at the electrolyte/Pt conducting interface and it is merged with  $R_{rec}$ . The obtained data are fitted with an equivalent circuit model and summarized in Table 3.

It was noted that  $R_{rec}$  for 3% In-doped samples was high, which implies reduced recombination dynamics in 3% In-doped DSSCs than in other devices. The  $R_s$  value represents the series resistance which contributes to the sheet resistance of FTO and the interface resistance of the anode material with the electrode. In the present study, the pure  $\text{SrSnO}_3/\text{TiO}_2$ -based device showed a very low  $R_s$  compared to indium-doped DSSCs. Employing a high dielectric material on FTO as a blocking layer increased the interface resistance of the DSSCs, which tends to an increase in the  $R_s$  value of doped samples. Moreover, the electron diffusion resistance ( $W_s$ ) at the photoanode is nearly the same owing to the defined and identical film thickness, and the  $R_d$  seems to be the same for all the DSSCs. Furthermore, the modification of electronic property  $\text{SrSnO}_3$  with indium doping enabled good electronic interaction through the  $\text{TiO}_2$  neighbor layer, which leads to enhanced charge transport properties.<sup>35,46</sup>

## CONCLUSIONS

The nanorods of pure and indium-doped  $\text{SrSnO}_3$  were effectively produced by the precipitation method. XRD and refined diffraction patterns disclose an orthorhombic  $\text{SrSnO}_3$  perovskite structure. Metal oxide (M–O) vibrations were analyzed through FTIR. The structural disorder persuaded by the indium (In) ions was explored through Raman spectra. Oxidation states, the shift in binding energies, and oxygen vacancies were confirmed by XPS. From electron microscopic analysis, pure  $\text{SrSnO}_3$  compounds exhibit a bundle of rods with

agglomeration, whereas all the indium-doped samples show a refined rod-like shape. The surface area analysis provides details of the pore size and specific surface area of the samples. The absorption spectra show an intense UV absorption and the addition of indium leads to a small variation in the optical energy ( $E_g$ ) gap. This explains the admirable optical behavior of indium-doped compounds. Multicolored emission suggested the presence of defect and vacancy states, which were identified by PL. Room temperature ferromagnetism was observed in pure and indium-doped  $\text{SrSnO}_3$  nanostructures. The ferromagnetic behavior of non-magnetic samples suggests that the defects and oxygen vacancies play a role in the magnetic phase transition. The efficiency of fabricated DSSCs with  $\text{SrSnO}_3$  as the blocking layer suggests that indium-doped samples are the most promising candidates to avoid the current leakage.

## ■ ASSOCIATED CONTENT

### SI Supporting Information

The Supporting Information is available free of charge at <https://pubs.acs.org/doi/10.1021/acsomega.2c01191>.

Crystal structure of  $\text{SrSnO}_3$  and  $W-H$  plot of  $\text{SrSnO}_3$  and indium-doped  $\text{SrSnO}_3$  nanostructures (PDF)

## ■ AUTHOR INFORMATION

### Corresponding Author

**Robin Jude Vimal Michael** – Kinetics and Catalysis Lab (KCL), Abdul Kalam Research Centre (AKRC), P. G. and Research Department of Chemistry, Sacred Heart College (Autonomous), Tirupattur 635601 Tamilnadu, India; [orcid.org/0000-0001-5238-3339](https://orcid.org/0000-0001-5238-3339); Email: [vimaljude@gmail.com](mailto:vimaljude@gmail.com)

### Authors

**Theanmozhi Mohan** – Kinetics and Catalysis Lab (KCL), Abdul Kalam Research Centre (AKRC), P. G. and Research Department of Chemistry, Sacred Heart College (Autonomous), Tirupattur 635601 Tamilnadu, India; [orcid.org/0000-0003-2004-1160](https://orcid.org/0000-0003-2004-1160)

**Sasikumar Kuppusamy** – Kinetics and Catalysis Lab (KCL), Abdul Kalam Research Centre (AKRC), P. G. and Research Department of Chemistry, Sacred Heart College (Autonomous), Tirupattur 635601 Tamilnadu, India; [orcid.org/0000-0002-6208-6458](https://orcid.org/0000-0002-6208-6458)

Complete contact information is available at: <https://pubs.acs.org/doi/10.1021/acsomega.2c01191>

### Notes

The authors declare no competing financial interest.

## ■ ACKNOWLEDGMENTS

The corresponding author Dr. R.J.V.M. and author T.M. acknowledges Sacred Heart College (Autonomous), Tirupattur, for the Don Bosco and Fr. Carreno Research Fellowship.

## ■ REFERENCES

- (1) Hagfeldt, A.; Boschloo, G.; Sun, L.; Kloo, L.; Pettersson, H. Dye-Sensitized Solar Cells. *Chem. Rev.* **2010**, *110*, 6595–6663.
- (2) Ito, S.; Murakami, T. N.; Comte, P.; Liska, P.; Grätzel, C.; Nazeeruddin, M. K.; Grätzel, M. Fabrication of thin film dye sensitized solar cells with solar to electric power conversion efficiency over 10%. *Thin Solid Films* **2008**, *516*, 4613–4619.
- (3) Chou, T. P.; Zhang, Q.; Fryxell, G. E.; Cao, G. Z. Hierarchically Structured ZnO Film for Dye-Sensitized Solar Cells with Enhanced Energy Conversion Efficiency. *Adv. Mater.* **2007**, *19*, 2588–2592.
- (4) Huang, L.; Jiang, L.; Wei, M. Metal-free indoline dye sensitized solar cells based on nanocrystalline  $\text{Zn}_2\text{SnO}_4$ . *Electrochim. Commun.* **2010**, *12*, 319–322.
- (5) Li, Y.; Pang, A.; Zheng, X.; Wei, M. CdS quantum-dot-sensitized  $\text{Zn}_2\text{SnO}_4$  solar cell. *Electrochim. Acta* **2011**, *56*, 4902–4906.
- (6) Minami, T.; Sonohara, H.; Takata, S.; Sato, H. Highly Transparent and Conductive Zinc-Stannate Thin Films Prepared by RF Magnetron Sputtering. *Jpn. J. Appl. Phys.* **1994**, *33*, L1693–L1696.
- (7) Kumar, R.; Sahoo, S.; Joanni, E.; Singh, R. K.; Maegawa, K.; Tan, W. K.; Kawamura, G.; Kar, K. K.; Matsuda, A. Heteroatom doped graphene engineering for energy storage and conversion. *Mater. Today* **2020**, *39*, 47–65.
- (8) Kumar, R.; da Silva, E. T. S. G.; Singh, R. K.; Savu, R.; Alafardov, A. V.; Fonseca, L. C.; Carossi, L. C.; Singh, A.; Khandka, S.; Kar, K. K.; Alves, O. L.; Kubota, L. T.; Moshkalev, S. A. Microwave-assisted synthesis of palladium nanoparticles intercalated nitrogen doped reduced graphene oxide and their electrocatalytic activity for direct-ethanol fuel cells. *J. Colloid Interface Sci.* **2018**, *515*, 160–171.
- (9) Kumar, R.; Singh, R. K.; Tiwari, R. S. Growth analysis and high-yield synthesis of aligned-stacked branched nitrogen-doped carbon nanotubes using sesame oil as a natural botanical hydrocarbon precursor. *Mater. Des.* **2016**, *94*, 166–175.
- (10) de Sousa Filho, I. A.; Arana, L. R.; Doungmo, G.; Grisolia, C. K.; Terrashke, H.; Weber, I. T.  $\text{SrSnO}_3/g\text{-C}_3\text{N}_4$  and sunlight: Photocatalytic activity and toxicity of degradation byproducts. *J. Environ. Chem. Eng.* **2020**, *8*, 103633.
- (11) Lee, C. W.; Kim, D. W.; Cho, I. S.; Park, S.; Shin, S. S.; Seo, S. W.; Hong, K. S. Simple synthesis and characterization of  $\text{SrSnO}_3$  nanoparticles with enhanced photocatalytic activity. *Int. J. Hydrogen Energy* **2012**, *37*, 10557–10563.
- (12) Misra, S.; Gnanasekar, K. I.; Rao, R. V. S.; Jayaraman, V.; Gnanasekaran, T. Electrical conductivity and oxygen sensing behavior of  $\text{SrSn}_{1-x}\text{Fe}_x\text{O}_{3-\delta}$  ( $x=0-0.2$ ). *J. Alloys Compd.* **2010**, *506*, 285–292.
- (13) Burnside, S.; Moser, J.-E.; Brooks, K.; Grätzel, M.; Cahen, D. Nanocrystalline Mesoporous Strontium Titanate as Photoelectrode Material for Photosensitized Solar Devices: Increasing Photovoltage through Flat band Potential Engineering. *J. Phys. Chem. B* **1999**, *103*, 9328–9332.
- (14) Tan, B.; Toman, E.; Li, Y.; Wu, Y. Zinc Stannate ( $\text{Zn}_2\text{SnO}_4$ ) Dye-Sensitized Solar Cells. *J. Am. Chem. Soc.* **2007**, *129*, 4162–4163.
- (15) Natu, G.; Wu, Y. Photoelectrochemical Study of the Ilmenite Polymorph of  $\text{CdSnO}_3$  and Its Photoanodic Application in Dye-Sensitized Solar Cells. *J. Phys. Chem. C* **2010**, *114*, 6802–6807.
- (16) Guo, F.-a.; Li, G.; Zhang, W. Barium Stannate as Semiconductor Working Electrodes for Dye-Sensitized Solar Cells. *Int. J. Photoenergy* **2010**, *2010*, 1.
- (17) Li, H.-Y.; Wu, J.; Huang, W.; Zhou, Y.-H.; Li, H.-R.; Zheng, Y.-X.; Zuo, J.-L. Synthesis and photoluminescent properties of five homodinuclear lanthanide ( $\text{Ln}^{3+}=\text{Eu}^{3+}$ ,  $\text{Sm}^{3+}$ ,  $\text{Er}^{3+}$ ,  $\text{Yb}^{3+}$ ,  $\text{Pr}^{3+}$ ) complexes. *J. Photochem. Photobiol., A* **2009**, *208*, 110–116.
- (18) Guo, H.; Chen, H.; Zhang, H.; Huang, X.; Yang, J.; Wang, B.; Li, Y.; Wang, L.; Niu, X.; Wang, Z. Low-temperature processed yttrium-doped  $\text{SrSnO}_3$  perovskite electron transport layer for planar heterojunction perovskite solar cells with high efficiency. *Nano Energy* **2019**, *59*, 1–9.
- (19) Bhat, A. A.; Zaman, M. B.; Malik, J. H.; Malik, K. A.; Assadullah, I.; Tomar, R. Facile Way of Making Hydrothermally Synthesized Crystalline  $\text{SrSnO}_3$  Perovskite Nanorods Suitable for Blue LEDs and Spintronic Applications. *ACS Omega* **2021**, *6*, 16356–16363.
- (20) Li, Y.; Zhang, H.; Guo, B.; Wei, M. Enhanced efficiency dye-sensitized  $\text{SrSnO}_3$  solar cells prepared using chemical bath deposition. *Electrochim. Acta* **2012**, *70*, 313–317.
- (21) Kumar, A. A.; Kumar, A.; Quamara, J. K.; Dillip, G. R.; Joo, S. W.; Kumar, J. Fe(III) induced structural, optical, and dielectric behaviour of cetyltrimethylammonium ammonium bromide stabilized

strontium stannate nanoparticles synthesized by a facile wet chemistry route. *RSC Adv.* **2015**, *5*, 17202–17209.

(22) Cho, T.-Y.; Ko, K.-W.; Yoon, S.-G.; Sekhon, S. S.; Kang, M. G.; Hong, Y.-S.; Han, C.-H. Efficiency enhancement of flexible dye-sensitized solar cell with sol–gel formed Nb<sub>2</sub>O<sub>5</sub> blocking layer. *Curr. Appl. Phys.* **2013**, *13*, 1391–1396.

(23) Lee, J. G.; Cheon, J. H.; Yang, H. S.; Lee, D. K.; Kim, J. H. Enhancement of Photovoltaic Performance in Dye-Sensitized Solar Cells with the Spin-Coated TiO<sub>2</sub> Blocking Layer. *J. Nanosci. Nanotechnol.* **2012**, *12*, 6026–6030.

(24) Kim, M.-H.; Kwon, Y.-U. Semiconductor CdO as a Blocking Layer Material on DSSC Electrode: Mechanism and Application. *J. Phys. Chem. C* **2009**, *113*, 17176–17182.

(25) Song, J.; Li, S. P.; Zhao, Y. L.; Yuan, J.; Zhu, Y.; Fang, Y.; Zhu, L.; Gu, X. Q.; Qiang, Y. H. Performance enhancement of perovskite solar cells by doping TiO<sub>2</sub> blocking layer with group VB elements. *J. Alloys Compd.* **2017**, *694*, 1232–1238.

(26) Wei, L.; Wang, P.; Yang, Y.; Dong, Y.; Fan, R.; Song, W.; Qiu, Y.; Yang, Y.; Luan, T. Enhanced performance of dye sensitized solar cells by using a reduced graphene oxide/TiO<sub>2</sub> blocking layer in the photoanode. *Thin Solid Films* **2017**, *639*, 12–21.

(27) Abdel-Galeil, M. M.; Kumar, R.; Matsuda, A.; El-Shater, R. E. Investigation on influence of thickness variation effect of TiO<sub>2</sub> film, spacer and counter electrode for improved dye-sensitized solar cells performance. *Optik* **2021**, *227*, 166108.

(28) Varandili, S. B.; Babaei, A.; Ataie, A. Characterization of B site co-doped LaFeO<sub>3</sub> nanoparticles prepared via co-precipitation route. *Rare Met.* **2018**, *37*, 181–190.

(29) Ouni, S.; Nouri, S.; Khemakhem, H.; Ben Hassen, R. Phase transitions, dielectric properties, and vibrational study of stannates perovskites Sr<sub>1-x</sub>Er<sub>x</sub>SnO<sub>3-δ</sub>. *Mater. Res. Bull.* **2014**, *51*, 136–140.

(30) Jin, S.; Hao, H.; Guo, W.; Yu, Y.; Hou, H.; Zhang, G.; Yan, S.; Gao, W.; Liu, G. Preparation and characterization of Sm<sup>3+</sup>-doped SrSnO<sub>3</sub> and its photoelectric performance as photo-anode of dye-sensitized solar cells. *J. Nanopart. Res.* **2017**, *19*, 279.

(31) Patel, D. K.; Rajeswari, B.; Sudarsan, V.; Vatsa, R. K.; Kadam, R. M.; Kulshreshtha, S. K. Structural, luminescence and EPR studies on SrSnO<sub>3</sub> nanorods doped with europium ions. *Dalton Trans.* **2012**, *41*, 12023–12030.

(32) Ahmed, J.; Blakely, C. K.; Bruno, S. R.; Poltavets, V. V. Synthesis of MSnO<sub>3</sub> (M = Ba, Sr) nanoparticles by reverse micelle method and particle size distribution analysis by whole powder pattern modelling. *Mater. Res. Bull.* **2012**, *47*, 2282–2287.

(33) Roh, K. S.; Ryu, K. H.; Yo, C. H. Nonstoichiometry and Physical Properties of the SrSn<sub>1-x</sub>Fe<sub>x</sub>O<sub>3-y</sub> System. *J. Solid State Chem.* **1999**, *142*, 288–293.

(34) de Freitas, S. M.; Júnior, G. J. B.; Santos, R. D. S.; dos S. Rezende, M. V. Defects and dopant properties of SrSnO<sub>3</sub> compound: A computational study. *Comput. Condens. Matter* **2019**, *21*, No. e00411.

(35) Ashok Kumar, K.; Pandurangan, A.; Arumugam, S.; Sathiskumar, M. Effect of Bi-functional Hierarchical Flower-like CoS Nanostructure on its Interfacial Charge Transport Kinetics, Magnetic and Electrochemical Behaviors for Supercapacitor and DSSC Applications. *Sci. Rep.* **2019**, *9*, 1228.

(36) Muralidharan, M.; Thiyagarajan, R.; Sivakumar, K.; Sivaji, K. Near infrared emission and enhanced ferromagnetism in Fe doped SrSnO<sub>3</sub> perovskite structured nanorods. *J. Mater. Sci.: Mater. Electron.* **2019**, *30*, 4634–4643.

(37) Rajamanickam, N.; Soundarajan, P.; Jayakumar, K.; Ramachandran, K. Improve the power conversion efficiency of perovskite BaSnO<sub>3</sub> nanostructures based dye-sensitized solar cells by Fe doping. *Sol. Energy Mater. Sol. Cells* **2017**, *166*, 69–77.

(38) Kennedy, B. J.; Qasim, I.; Knight, K. S. Low temperature structural studies of SrSnO<sub>3</sub>. *J. Phys.: Condens. Matter* **2015**, *27*, 365401.

(39) Alves, M. C. F.; Nascimento, M. R.; Lima, S. J. G.; Pizani, P. S.; Espinosa, J. W. M.; Longo, E.; Soledade, L. E. B.; Souza, A. G.; Santos,

I. M. G. Influence of synthesis conditions on carbonate entrapment in perovskite SrSnO<sub>3</sub>. *Mater. Lett.* **2009**, *63*, 118–120.

(40) Alves, M. C. F.; Souza, S. C.; Lima, H. H. S.; Nascimento, M. R.; Silva, M. R. S.; Espinosa, J. W. M.; Lima, S. J. G.; Longo, E.; Pizani, P. S.; Soledade, L. E. B.; Souza, A. G.; Santos, I. M. G. Influence of the modifier on the short and long range disorder of stannate perovskites. *J. Alloys Compd.* **2009**, *476*, 507–512.

(41) Moreira, E.; Henriques, J. M.; Azevedo, D. L.; Caetano, E. W. S.; Freire, V. N.; Albuquerque, E. L. Structural, optoelectronic, infrared and Raman spectra of orthorhombic SrSnO<sub>3</sub> from DFT calculations. *J. Solid State Chem.* **2011**, *184*, 921–928.

(42) Muralidharan, M.; Anbarasu, V.; Elaya Perumal, A.; Sivakumar, K. Room temperature ferromagnetism in Cr doped SrSnO<sub>3</sub> perovskite system. *J. Mater. Sci.: Mater. Electron.* **2017**, *28*, 4125–4137.

(43) Alammar, T.; Hamm, I.; Grasmik, V.; Wark, M.; Mudring, A.-V. Microwave-Assisted Synthesis of Perovskite SrSnO<sub>3</sub> Nanocrystals in Ionic Liquids for Photocatalytic Applications. *Inorg. Chem.* **2017**, *56*, 6920–6932.

(44) Singh, D. J.; Xu, Q.; Ong, K. P. Strain effects on the band gap and optical properties of perovskite SrSnO<sub>3</sub> and BaSnO<sub>3</sub>. *Appl. Phys. Lett.* **2014**, *104*, 011910.

(45) Bramhankar, T. S.; Pawar, S. S.; Shaikh, J. S.; Gunge, V. C.; Beedri, N. I.; Baviskar, P. K.; Pathan, H. M.; Patil, P. S.; Kambale, R. C.; Pawar, R. S. Effect of Nickel–Zinc Co-doped TiO<sub>2</sub> blocking layer on performance of DSSCs. *J. Alloys Compd.* **2020**, *817*, 152810.

(46) Rajamanickam, N.; Soundarajan, P.; Senthil Kumar, S. M.; Jayakumar, K.; Ramachandran, K. Boosting photo charge carrier transport properties of perovskite BaSnO<sub>3</sub> photoanodes by Sr doping for enhanced DSSCs performance. *Electrochim. Acta* **2019**, *296*, 771–782.